

ARTICLE

Received 11 Aug 2015 | Accepted 3 Dec 2015 | Published 27 Jan 2015

DOI: 10.1038/ncomms10386

OPEN

Polaronic metal state at the $\text{LaAlO}_3/\text{SrTiO}_3$ interface

C. Cancellieri^{1,2,*}, A.S. Mishchenko^{3,*}, U. Aschauer^{4,5}, A. Filippetti⁶, C. Faber⁴, O.S. Barišić⁷, V.A. Rogalev¹, T. Schmitt¹, N. Nagaosa^{3,8} & V.N. Strocov^{1,*}

Interplay of spin, charge, orbital and lattice degrees of freedom in oxide heterostructures results in a plethora of fascinating properties, which can be exploited in new generations of electronic devices with enhanced functionalities. The paradigm example is the interface between the two band insulators LaAlO_3 and SrTiO_3 that hosts a two-dimensional electron system. Apart from the mobile charge carriers, this system exhibits a range of intriguing properties such as field effect, superconductivity and ferromagnetism, whose fundamental origins are still debated. Here we use soft-X-ray angle-resolved photoelectron spectroscopy to penetrate through the LaAlO_3 overlayer and access charge carriers at the buried interface. The experimental spectral function directly identifies the interface charge carriers as large polarons, emerging from coupling of charge and lattice degrees of freedom, and involving two phonons of different energy and thermal activity. This phenomenon fundamentally limits the carrier mobility and explains its puzzling drop at high temperatures.

¹Swiss Light Source, Paul Scherrer Institute, Villigen CH-5232, Switzerland. ²EMPA, Swiss Federal Laboratories for Materials Science & Technology, Ueberlandstrasse 129, Dübendorf 8600, Switzerland. ³RIKEN Center for Emergent Matter Science, 2-1 Hirosawa, Wako, Saitama 351-0198, Japan. ⁴Materials Theory, ETH Zurich, Wolfgang-Pauli-Strasse 27, Zürich CH-8093, Switzerland. ⁵Department of Chemistry and Biochemistry, University of Bern, Freiestrasse 3 3012 Bern, Switzerland. ⁶CNR-IOM, Istituto Officina dei Materiali, Cittadella Universitaria, Cagliari, Monserrato 09042-I, Italy. ⁷Institute of Physics, Bijenička 46, 10000 Zagreb, Croatia. ⁸Department of Applied Physics, The University of Tokyo, 7-3-1 Hongo, Bunkyo-ku, Tokyo 113-8656, Japan. * These authors contributed equally to this work. Correspondence and requests for materials should be addressed to V.N.S. (email: vladimir.strocov@psi.ch).

Coupling of the electron and lattice degrees of freedom in solids through electron–phonon interaction (EPI) is a key concept in electron transport and many other phenomena of condensed matter physics. An electron moving in the lattice can displace atoms from their equilibrium positions in response to the EPI. Such an electron (or hole) dragging behind a local lattice distortion—or phonon ‘cloud’—forms a composite charge carrier known as polaron^{1,2}. The increased effective mass m^* of this quasi-particle (QP) fundamentally limits its mobility $\mu \propto 1/m^*$ beyond incoherent scattering processes. The polarons are key players in many technological devices, a widespread example of which are high-electron mobility transistors (HEMTs) utilized in high-frequency devices such as mobile phones. In typical HEMTs, a donor layer of n-doped AlGaAs injects electrons into the channel layer of intrinsic GaAs where, escaping scattering on the dopant impurities, the electrons are limited in their mobility only by the polaronic coupling enhanced by spatial confinement in the GaAs quantum well (QW)³.

Angle-resolved photoelectron spectroscopy (ARPES) is a unique method to measure the single particle spectral function $A(\omega, \mathbf{k})$ in crystalline solids resolved in electron energy ω and momentum \mathbf{k} . Containing all many-body (electron–electron, electron–phonon, and so on) interactions, $A(\omega, \mathbf{k})$ reveals the formation of polarons by a characteristic peak-dip-hump (PDH) lineshape, where the sharp peak corresponds to a QP and the broad hump, extending to higher binding energies, corresponds to the cloud of entangled phonons with frequencies ω_0 (refs 1,2). However, the extreme surface sensitivity of conventional ARPES with photon energies $h\nu$ below ~ 100 eV sets the buried interfaces out of its reach. The crucial feature of our experiment is the use of soft-X-ray ARPES (SX-ARPES) operating in the $h\nu$ range of hundreds eV (for a recent review see ref. 4). The longer photoelectron mean free path enables SX-ARPES to penetrate through the top layers and access $A(\omega, \mathbf{k})$ at buried interfaces.

Complex oxide interfaces are presently at the forefront of fundamental research in view of their enhanced functionalities achieved by exploiting electron correlations^{5,6}. The two-dimensional electron system (2DES) in $\text{LaAlO}_3/\text{SrTiO}_3$ (LAO/STO)⁷ is confined within a narrow region of a few nanometres on the STO side^{8–10}, where the mobile electrons populate the t_{2g} -derived d_{xy} -, d_{xz} - and d_{yz} -states of Ti ions acquiring reduced valence compared with bulk Ti^{4+} . Confinement in the interface QW further splits these states into a ladder of subbands^{8,11–14}. This complex energy structure based on the correlated $3d$ orbitals, very different from conventional semiconductor heterostructures described as free particles embedded in the mean-field potential, is the source of a rich and non-trivial phenomenology. Here high 2DES mobility μ_{2DES} typical of uncorrelated ESs co-exists with superconductivity^{5,6}, ferromagnetism^{15,16}, large magnetoresistance¹⁷ and other phenomena typical of localized correlated electrons. Other intriguing puzzles in this intricate physics are why μ_{2DES} measured in transport falls short of estimates based on mean-field theories, and what causes the dramatic drop of μ_{2DES} with increase of temperature¹⁸.

Here, we directly access the nature of the LAO/STO interface carriers through their $A(\omega, \mathbf{k})$ measured by SX-ARPES at ultrahigh-energy resolution. We discover that the LAO/STO interface forms a polaronic metal state involving at least two active phonons. While polaronic coupling to hard LO3 phonons fundamentally limits μ_{2DES} at low temperatures, coupling to soft TO1 phonons with increasing temperature provides the microscopic mechanism of μ_{2DES} drop observed in transport.

Results

Spectroscopic signatures of the polaronic metal state. Our LAO/STO(001) samples with an LAO overlayer thickness of ~ 18 Å corresponding to 5 unit cells (u.c.) were grown using Pulsed Layer Deposition (PLD), and subsequently annealed in oxygen atmosphere to minimize the concentration of oxygen vacancies (V_{OS}) and the related extrinsic charge carriers^{7,19}. SX-ARPES with its crucial advantage of enhanced probing depth is ideally suited to study this buried system where the 2DES only develops with the LAO layer thickness > 3 u.c. (ref. 20) The extremely small 2DES signal, however, has to be boosted using resonant photoemission²¹ locked to the interface Ti ions^{14,22,23}. For details of the sample growth and SX-ARPES experiment, see Methods.

Our low-temperature experimental data set in Fig. 1 was measured at 12 K using *s*-polarized X-rays (the parallel *p*-polarization data are given in the Supplementary Note 1). The resonance map of (angle-integrated) photoemission intensity, Fig. 1a, was recorded under variation of $h\nu$ across the Ti 2*p* absorption edge ~ 460 eV. We identify there the 2DES signal at the Fermi level E_F blowing up near the two Ti^{3+} L_3 - and L_2 -resonances and vanishing everywhere else (we notice that strong suppression of the in-gap states around -1.2 eV, related to the V_{OS} (refs 14,22,23), confirms the prevalence of the intrinsic interface charge carriers). Tuning $h\nu$ onto the stronger L_3 -resonance produces the Fermi surface (FS) map in Fig. 1b where, by comparison with the superimposed theoretical FS contours, we recognize the manifold of merged circular d_{xy} -derived FS sheets and the elliptical d_{yz} -sheet extending in the k_x -direction^{14,23}.

The ARPES images measured along the ΓX ($k_y = 0$) line of the square 2D Brillouin zone (BZ) at the L_3 - and L_2 -resonances are shown in Fig. 2a,b, respectively. With a high-energy resolution of 40 meV, these images resolve individual interface bands. The use of *s*-polarization selects the d_{xy} - and d_{yz} -derived states, which are antisymmetric relative to the ΓX line¹⁴ (although the selection rules are slightly relaxed by remnant structural distortions). By comparison with the overlaid $E(\mathbf{k})$ dispersions calculated for LAO/STO interface with pseudo-self-interaction correction DFT (see Methods) one can recognize the lower d_{yz} -band with its flat dispersion. Already at this point, we note signs of a QP interaction, which reduces the band dispersion compared with the overlaid DFT prediction as characterized by an effective mass ratio of $m^*/m_0 \sim 2.5$. The d_{xy} -bands are not visible due to vanishing matrix elements, but the lowest d_{xy} -band appears as two bright spots where it hybridizes with the d_{yz} -band.

The most striking visual aspect of the experimental $E(\mathbf{k})$ is, however, the two vertical waterfalls extending down from these

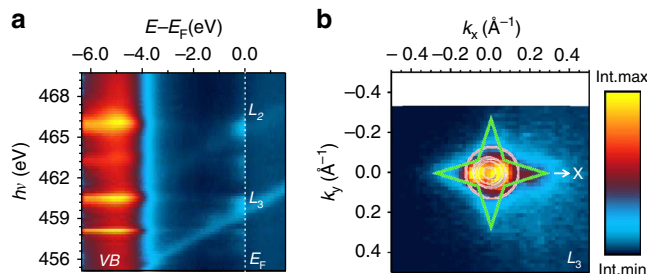


Figure 1 | Experimental low-temperature (12 K) overview SX-ARPES data. (a) Resonance (angle-integrated) photoemission intensity map, identifying the 2DES signal at the L_3 and L_2 resonances of the interface Ti ions. (b) FS map at the L_3 -resonance, where the superimposed theoretical FS contours identify the d_{xy} (pink) and d_{yz} (green) sheets. The colour bar indicates the intensity (Int.) maximum and minimum.

high-intensity d_{xy} spots. In Fig. 2c,d we show the energy distribution curves (EDCs)—that is, ARPES intensity as a function of binding energy for a given \mathbf{k} —extracted from the images in Fig. 2a,b, respectively. These EDCs reveal, remarkably, a pronounced PDH structure of $A(\omega, \mathbf{k})$, where the peak reflects the QP and the hump at ~ 118 meV below the peak its coupling to bosonic modes (such as magnon, plasmon, phonon) whose nature will be identified later on.

We note in passing that the EDC representing the whole d_{xy} -band, Fig. 2c, exhibits a smaller but broader QP peak in comparison to its d_{yz} -counterpart in Fig. 2d. Their nearly equal integral QP weight indicates that, non-trivially, the bosonic coupling is quite insensitive to different spatial distribution of the d_{xy} - and d_{yz} -states⁸. The larger broadening of d_{xy} -EDC can reflect larger defect scattering, because the lowest d_{xy} -state is localized closest to the interface where the concentration of defects generated by the non-equilibrium PLD growth is maximal, whereas the d_{yz} -state extends deeper into the defect-free STO bulk. This observation is consistent with the recent Shubnikov–de

Haas experiments¹⁵, which have found smaller d_{xy} -mobility compared with $d_{xz/yz}$ -one.

We will now address the nature of the involved bosonic modes. Considering the extremely small ferromagnetic response of the LAO/STO interface¹⁵, the magnons can safely be ruled out. Plasmons can also be excluded since the energy of the hump does not depend on the interfacial carrier concentration n_s varied via manipulation of V_{OS} (see Supplementary Note 2) while the plasma frequency ω_p is proportional to $\sqrt{n_s}$. These bosonic modes can therefore be assigned to phonons coupling to electron excitations and forming polarons^{24–26}. The hump apex, located at ~ 118 meV below the QP peak, identifies the main coupling phonon frequency ω_0' . The 2DES at the LAO/STO interface realizes therefore a polaronic metal state.

To identify the phonon modes forming the observed polaron, we used DFT to calculate the phonon dispersions (see Methods) for cubic bulk STO at different electron doping concentrations n_v ; the results are shown in Fig. 3a. Although these initial calculations are for cubic STO, we will address shifts of the phonon frequencies at the cubic to tetragonal phase transition when discussing the temperature dependence. The $\frac{\partial \omega_0}{\partial n_v}$ response of the calculated dispersions quantifies the EPI strength as a function of phonon mode and \mathbf{q} . With the actual electron density distribution^{8–10}, our n_s measured by the Luttinger area of the experimental FS roughly corresponds to $n_v = 0.12$ electrons per u.c. Since the carriers reside on the STO side of the LAO/STO interface, we expect these results to be relevant for the interface as well. The polaron can be associated with the hard longitudinal optical phonon LO3, which is the only mode available in this high-energy range and, moreover, has the largest coupling constant λ among all LO modes^{27,28} as observed by Raman²⁹ and neutron spectroscopy³⁰. At finite \mathbf{q} vectors, the LO3 mode

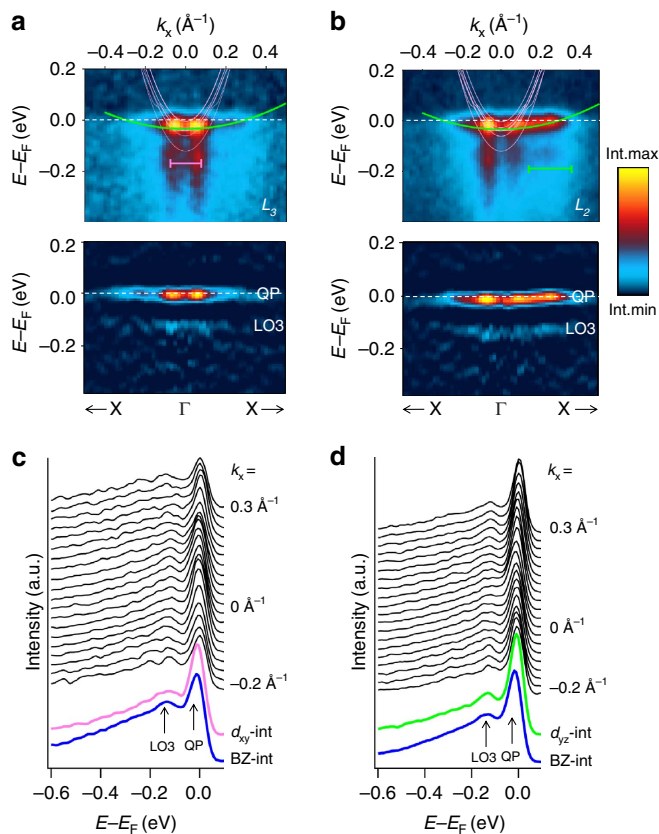


Figure 2 | Experimental low-temperature (12 K) high-resolution SX-ARPES. (a,b) High-resolution ARPES images along the ΓX ($k_y = 0$) line at the L_3 - and L_2 -edges, respectively, with the superimposed theoretical d_{xy} (pink) and d_{yz} (green) bands. The lower panels show the corresponding second derivative $-d^2I/dE^2 > 0$ plots, which clearly show both the quasi-particle (QP) peak and the dispersive hump formed by the LO3 phonon. (c,d) A series of (normalized) EDCs extracted from a,b respectively, at the indicated k_x -values through the occupied part of the BZ. The colour bar indicates the intensity maximum and minimum. The two curves at the bottom show EDCs integrated over the \mathbf{k} -ranges indicated in c,d as well as the whole BZ in the k_x -direction. The characteristic PDH spectral structure in c,d manifests a polaronic metal state formed by the hard LO3 phonon and renormalizing the d_{yz} -band dispersion in a,b and the clear hump dispersion in b identifies a large polaron.

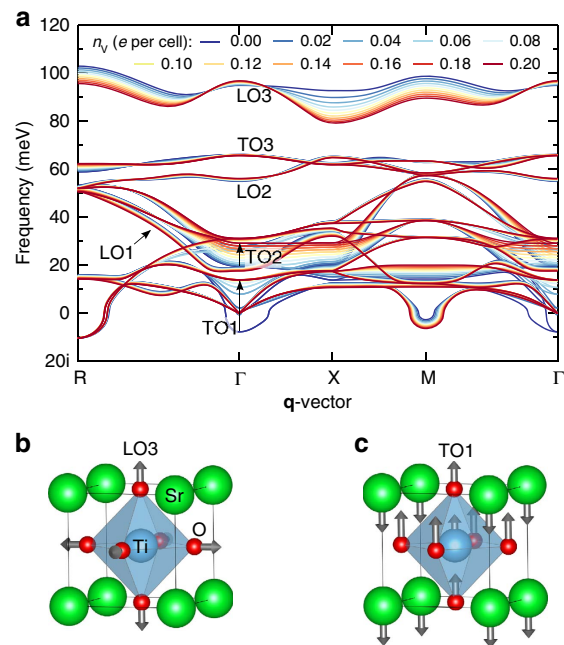


Figure 3 | Theoretical phonon modes in cubic phase doped STO.

(a) Phonon dispersion at various electron doping levels n_v , with our case corresponding to $n_v \sim 0.12$. The arrows indicate the TO1 and TO2 modes shifting as a function of n_v . The imaginary modes at the R- and M-points represent different octahedral rotation instabilities, whereas the one at the Γ -point in the undoped materials is the polar (quantum-paraelectric) instability. (b,c) Atomic displacements associated with the breathing LO3 mode at the R-point and the polar TO1 mode at the Γ -point, respectively.

represents a breathing distortion of the octahedral cage around a Ti site, Fig. 3b, which is typical of polaron formation driven by the (Holstein-type) short-range EPI, barely sensitive to electron screening in a metallic system. This character of EPI is confirmed by the increase of $\frac{\partial\omega_n}{\partial n_V}$ with increase of \mathbf{q} away from the Γ -point. Recent optical studies on bulk STO³¹ have not only confirmed the involvement of the LO3 phonon in EPI but also found the corresponding effective mass renormalization $m^*/m_0 \sim 3.0$ close to our value. This mode has also been observed by ARPES on (doped) bare STO(001)^{32–34} with the strength of the polaronic structure depending on n_s . We note that, our theoretical LO3 energy of ~ 100 meV perfectly matches that found experimentally for the bare STO bulk and surface, but it differs from our $\omega_0' \sim 118$ meV measurement at the LAO/STO interface. To gain some insight on this discrepancy, we investigated the possible role of strain by performing additional calculations with the STO in-plane lattice constants constrained to that of LAO. However, only a minor frequency shift to 102 meV was found. This implies that other interfacial factors such as the electric field, phonon coupling across the interface, propagation of the LAO distortion into STO³⁵, structural changes due to electrostatic doping³⁶ or weaker coupling to additional phonon modes could also play a role. We also note that the EPI at LAO/STO is enhanced by the tight 2D electron confinement in the interface QW^{2,3}, which was recently evidenced by huge oscillations of thermopower as a consequence of large phonon drag³⁷.

Next, we perform a theoretical analysis of the PDH structure to estimate the strength of the EPI governing the polaron formation. With the total $A(\omega, \mathbf{k})$ spectral weight normalized to unity, we define Z_0 as the integral weight of the QP part. The observed $A(\omega, \mathbf{k})$ of a polaron with momentum \mathbf{k} can be expressed as a sum of two terms^{1,2}

$$A(\omega, \mathbf{k}) = Z_0 \delta[\omega - E(\mathbf{k})] + A^H(\omega, \mathbf{k}) \quad (1)$$

The first term represents the sharp QP peak with the dispersion $E(\mathbf{k})$ and effective mass m^* resulting from the renormalization of the non-interacting single-particle band with dispersion $\varepsilon(\mathbf{k})$ and mass m^0 . The second term arises due to phonons coupling to the excited photohole. The EPI has a twofold effect on $A(\omega, \mathbf{k})$: it reduces Z_0 below unity, and builds up $A^H(\omega, \mathbf{k})$, with its dispersion following $\varepsilon(\mathbf{k})$, as a Frank-Condon series of phonon peak replicas at energy separations $\omega_n = n\omega_0$ from the QP peak, where ω_0 is the phonon frequency and n indexes the replicas.

For our analysis, we used the angle-integrated EDC at the L_3 -resonance (Fig. 2c), which is dominated by the d_{xy} -intensity and thus insensitive to the dispersion effects in the d_{yz} -band (certain admixture of the latter is not important because its dispersion range is much smaller than our experimental resolution of 40 meV and, moreover, the d_{xy} - and d_{yz} -bands have the same peak-to-hump relative weight). Gaussian fitting of its QP peak yields $Z_0 \sim 0.4$. For the short-range EPI, forming the LO3 polaron, exact diagrammatic quantum Monte Carlo (QMC) calculations³⁸ have shown that the relation $m^*/m_0 \sim 1/Z_0$ holds with high accuracy. With the determined Z_0 , this yields $m^*/m_0 = 2.5$, which coincides with the value extracted above from the band dispersions, leaving not much room for electron correlations to contribute to the band renormalization. The latter is confirmed by theoretical analysis of tunnelling experiments³⁹ where the local electron correlations were described with the Hubbard parameter U . According to (ref. 40), already at $U = 4t$ (t is the hopping integral) the density of states significantly renormalizes and forms a pseudogap at E_F . The absence of the latter in the tunnelling spectra³⁹ indicates $U < 4t$. Then the renormalization exponent extracted from the correlation effects $m^*/m_0 = [1 - (U/U_c)^2]^{-1}$ ($U_c = 8t$ is the critical Mott value) is < 1.3 , which is much smaller than our experimental m^*/m_0 .

Hence, the mass renormalization at the LAO/STO interface is dominated by EPI.

Furthermore, the coupling strength λ for our short-range EPI can be estimated as $\lambda \sim 1 - Z_0$, which yields $\lambda \approx 0.6$. This value is well-below the limit $\lambda \sim 0.9$ separating the weak- and strong-coupling regimes, which implies that we observe large polarons, where the lattice distortion extends over several unit cells^{1,2,41}. This is perfectly consistent with the clear dispersion of the hump, which tracks the non-interacting $\varepsilon(\mathbf{k})$ dispersion of the d_{yz} -band in Fig. 2d. Importantly, the small λ also excludes that self-trapping of small polarons^{42,43} can be responsible for the discrepancy between the observed mobile charge and the 0.5 electrons per u.c. required for full compensation of the polar field in the LAO overlayer^{5,6,43}. However, the EPI can assist charge trapping on shallow defects⁴⁴ created by non-equilibrium PLD growth or V_{OS} , in addition to the deep level trapping.

The polaronic reduction of μ_{2DES} fundamentally limits the application potential of the STO-based heterostructures. As illustrated in Supplementary Note 2, this limit can possibly be circumvented through manipulation of V_{OS} . The V_{OS} inject into the 2DES extrinsic charge carriers⁴³, which increase the electron screening and thus reduce the EPI. This trend is consistent with the recent study at bare STO(100) surfaces³³ and, furthermore, explains the recent results on the γ -Al₂O₃/STO⁴⁵, where the V_{OS} have not only increased n_s but also μ_{2DES} by almost 2 orders of magnitude. On the other hand, the V_{OS} can assist the EPI due to charge trapping on shallow defects⁴⁴ and also increase the defect scattering rate, both effects counteracting the above positive trend. Further experiments on oxygen-deficient LAO/STO will allow a better understanding of the role of V_{OS} and ways to optimize μ_{2DES} .

Temperature dependence of polaronic effects. An intriguing peculiarity of the charge carriers at the LAO/STO interface is the drop of μ_{2DES} by more than 1 order of magnitude as the temperature increases above 200 K (ref. 18). To unveil the underlying microscopic mechanism, we measured the temperature dependence of the L_3 angle-integrated EDC from Fig. 2c (the angle integration makes our analysis robust against extrinsic thermal scattering of high-energy photoelectrons, which averages the ARPES signal in \mathbf{k} -space⁴⁶). These results are shown in Fig. 4a in comparison with experimental temperature dependence of μ_{2DES} in Fig. 4b, characteristic of the LAO/STO samples¹⁸, which was derived from Hall effect measurements. The experimental $A(\omega, \mathbf{k})$ in Fig. 4a shows that with increase of temperature, first, the polaronic hump broadens and propagates to higher binding energies. This trend is accompanied by increase of the QP peak width, Fig. 4d. These effects can be attributed to incoherent scattering on thermally populated phonon modes. A striking effect beyond this weight-conserving mechanism is, however, that the QP peak loses its integral weight Z_0 (Fig. 4c) and completely dissolves in the phonon hump of $A(\omega, \mathbf{k})$ towards 190 K (Fig. 4a). The decrease of Z_0 , following the trend of the temperature-dependent μ_{2DES} , unambiguously signals that the QP spectral weight leaks to soft phonon modes, different from the hard LO3, with concomitant further increase of m^* . This phenomenon provides the microscopic mechanism of the puzzling μ_{2DES} drop with increasing temperature^{18,41}. Interestingly, ARPES on the TiO₂(001) surface shows similar temperature effects²⁴ despite different crystallographic structure of TiO₂. In line with our results, an optical study of bulk STO³¹ has also revealed reduction of the Drude weight with temperature. Surprisingly, the bare STO(100) surface at large n_v (ref. 32) does not show any systematic

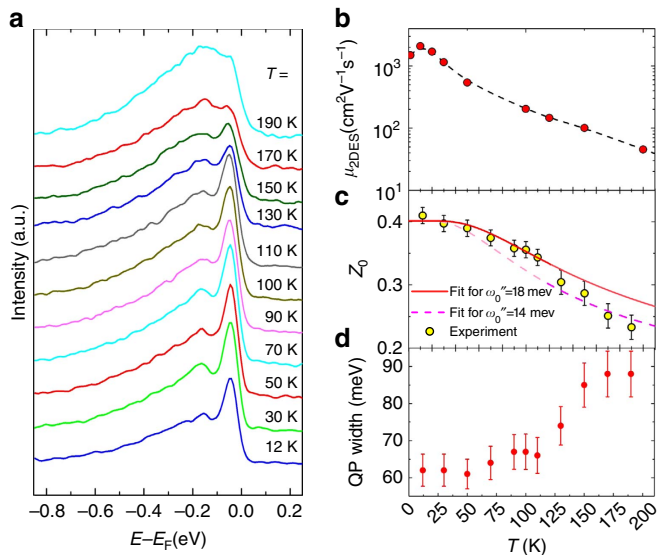


Figure 4 | Temperature dependence of polaronic effects. (a) Angle-integrated EDCs at the L_3 -resonance acquired for temperatures between 12 and 190 K. The QP peak dissolving into the hump towards ~ 190 K explains (b) the mobility drop with temperature measured in transport (the dashed line trends through the experimental points). (c) Temperature-dependent QP spectral weight $Z_0(T)$ fitted by the independent boson model of equation (2). The fit identifies a soft phonon mode (likely the TO1) with $\omega_0'' = 18$ meV (solid line) in the low- T region, which shifts to $\omega_0'' = 14$ meV (dashed) in the high- T region through the tetragonal to cubic phase transition in STO. The fading colours represent the validity ranges of the fits. (d) QP peak width (including the instrumental resolution). The error bars in c,d correspond to the uncertainty in the Gaussian fit of the QP.

temperature effects in the QP weight; clearly, the LAO overlayer and 2DES significantly alter the EPI in the LAO/STO system.

Numerical analysis of the temperature-dependent ARPES spectral shape allows us to identify the frequency ω_0'' of the soft phonon mode dominating the EPI. From the normalized EDCs, Fig. 4a, we evaluate the temperature dependence of the spectral weight $Z_0(T)$ by Gaussian fitting of the QP peak. The resulting $Z_0(T)$ in Fig. 4c can then be fitted with the analytic formula for the independent boson model¹

$$Z_0(T) = e^{-2g(2N+1)} I_0[2g(2N+1)], \quad (2)$$

where $N = (e^{\omega_0/T} - 1)^{-1}$ is the Bose filling factor, which describes the population number as a function of the mode frequency ω_0 at T , and I_0 is the modified Bessel function. This equation, neglecting momentum dependence and thus valid for our momentum-integrated EDCs, describes transfer of the spectral weight from the QP peak to the hump with temperature. The constant g -factor, measuring the EPI strength, was set to 0.95 to reproduce the experimental value $Z_0(12\text{K}) \sim 0.4$. Fitting $Z_0(T)$ in the temperature range below ~ 120 K yields $\omega_0'' \approx 18$ meV (solid line in Fig. 4c), while the high- T range yields $\omega_0'' \sim 14$ meV (dashed line in Fig. 4c). This crossover of ω_0'' can be linked to the second-order tetragonal to cubic phase transition in STO at 105K (refs 32,47). One may therefore argue that the μ_{2DES} drop in LAO/STO has structural origin. Interestingly, the fastest change of the QP peak width in Fig. 4d falls into the same temperature region. All other possible temperature effects in the QP linewidth, including the Bloch-Grüneisen contribution due to acoustic phonons, are weaker for our system dominated by the optical phonon, and obscured by the phase transition and limited energy resolution. We note that, strictly speaking, our $Z_0(T)$ model (2) had to include EPI with

both low- and high-energy phonons, contributing to the total EPI. However, the result would not change significantly because the Bose filling factor N , determining the $Z_0(T)$ dependence, is most sensitive to small ω_0 . In other words, the $Z_0(T)$ dependence is most sensitive to the low-energy sector of the phonon spectrum.

Next we return to our DFT calculations to identify the observed soft ω_0'' phonon mode. The phonon dispersions of the cubic (high- T) phase, Fig. 3a, show a multitude of low-energy modes. The lowest energy LO mode (LO1), which was previously linked with kinks in ARPES dispersions²⁸, has an energy of ~ 22 meV. This energy is considerably higher than our high- T fitted $\omega_0'' \sim 14$ meV and, moreover, our calculations do not show a significant frequency difference between the cubic and tetragonal phases of STO. These facts, together with the reported small coupling constant λ (ref. 27), make the involvement of this LO1 mode unlikely. In Fig. 3a we see, however, the TO modes strongly affected by the electron doping n_v due to enhanced screening. The TO1 mode, sketched in Fig. 3c, is a polar mode whose instability in undoped STO leads to its quantum-paraelectric behaviour^{48,49}. Its frequency rapidly increases and becomes real with increase of n_v , stabilizing above our actual $n_v \sim 0.12$ electrons per u.c. at $\omega_{\text{TO1}} \sim 13.7$ meV at the Γ point. This ω_{TO1} matches well with our $\omega_0'' \sim 14$ meV fitted in the high- T range. Turning to the low- T range, previous calculations on undoped STO have shown that the tetragonal phase transition increases ω_{TO1} (ref. 50). Our computations with $n_v = 0.12$ electrons per u.c. for the tetragonal phase indeed show ω_{TO1} to shift to 15.3 meV for the doubly degenerate mode and 18.1 meV for the non-degenerate mode along the octahedral rotation axis, which is in good agreement with our low- T fitted value $\omega_0'' \sim 18$ meV. Octahedral rotations different from this bulk tetragonal distortion were observed at the LAO/STO interface due to electrostatic doping^{35,36}, but since they are combinations of distortions similar to the one studied here, they are expected to also lead to an upwards shift of the TO1 frequency. Based on the t_{1u} symmetry of the TO1 mode, its good agreement with the experimental ω_0'' and its sensitivity to the cubic to tetragonal phase transition, we associate the experimental soft phonon with TO1. Moreover, significant polaronic coupling to this polar mode is consistent with gigantic dielectric constant ϵ_0 of STO caused by large polar ionic displacements under electric field in this material on the verge of a ferroelectric instability³⁰. The TO1 mode is associated with long-range EPI, as evidenced by the increase of $\frac{\partial \omega_0}{\partial n_v}$ towards the Γ -point. The hard LO3 and soft TO1 modes involved in the polaron formation are therefore associated with opposite types of EPI. The EPI strength in the latter case can be estimated from the Fröhlich model which, although strictly valid only for the polar LO modes, represents the only viable model to find the long-range coupling constant α . Based on exact diagrammatic QMC calculations⁵¹ and Z_0 at the top of our temperature range, we estimate $\alpha \approx 2$ for the TO1 mode. Similar to the above LO3 phonon, this value stays below the weak- to strong-coupling crossover at $\alpha \approx 6$, which implies that the TO1 phonon is also consistent with the large polaron scenario. We note that if LAO/STO superconductivity is driven by a phonon mechanism⁵², it can be related to the discovered polaronic activity. While the hard LO3 phonon energy much exceeds the energy scale of the superconducting transition at 0.3 K, involved in the electron pairing may be the soft TO1 phonon.

The 2DES at the LAO/STO interface realizes thus a polaronic metal state involving at least two phonons with different energies and thermal activity. The hard LO3 phonon at $\omega_0' \sim 118$ meV, associated with short-range EPI, is directly resolved as the characteristic hump in the experimental $A(\omega, \mathbf{k})$. It sets the fundamental limit of μ_{2DES} at low temperature, and exhaustively

accounts for the m^* renormalization without notable effects of electron correlations. Another soft phonon, likely the TO1 one associated with long-range EPI, changes its frequency from $\omega_0'' \sim 18$ to 14 meV across the phase transition in STO. This phonon causes a dramatic fading of the QP weight with temperature as the microscopic mechanism behind the μ_{2DES} drop observed in transport. The two phonons form a large polaron characterized by a lattice deformation extending over several unit cells. Physically, the involvement of both LO3 and TO1 phonons in the polaronic state means that the corresponding lattice distortion combines both breathing and polar atomic displacements. The polaronic activity is typical of oxide perovskites, reflecting their highly ionic character and easy structural transformations^{30,42}. Our discovery may have implications for other related oxide systems, including LAO/STO interfaces with different crystallographic orientations. In a methodological perspective, we have demonstrated the power of the newly emerging experimental technique of ultrahigh-resolution SX-ARPES to retrieve information about polaronic effects at buried interfaces in the most direct way as embedded in one-electron $A(\omega, \mathbf{k})$.

Methods

Sample preparation. Our LAO/STO samples were grown using PLD (for details of the growth procedure see refs 19,22) and subsequently annealed in oxygen atmosphere with a pressure of 200 mBar at 550 °C for 1 h to minimize the concentration of V_{Os} . These vacancies manifest themselves in ARPES spectra as characteristic dispersionless in-gap states at a binding energy of ~ 1.2 eV (refs 14,22) which, similar to bare STO, grow with exposure to X-rays. Our resonant spectra in Fig. 1a show only traces of such spectral structures enhanced at the $Ti^{3+} L_{3-}$ and L_{2-} resonances, indicating negligible concentration of V_{Os} . Measurements on samples with various n_s varied through the V_{Os} (Supplementary Note 2) demonstrated constant energy of the 118-meV spectral peak, excluding its plasmonic origin. The temperature-dependent mobility data were derived from standard Hall effect and conductivity measurements performed in the van der Paw geometry on square samples.

SX-ARPES experiment. SX-ARPES experiments were performed at the ADDRESS beamline of the Swiss Light Source, Paul Scherrer Institute, Switzerland⁵³. The experimental geometry allows symmetry analysis of the valence states using variable linear polarizations of incident X-rays. The experiments are normally performed at low sample temperatures ~ 12 K to quench thermal scattering of high-energy photoelectron destructive for the coherent \mathbf{k} -resolved spectral component⁴⁶. The combined (beamline and analyser) energy resolution was set to 80 meV for measurements of the FS, and to 40 meV for high-resolution measurements of the band dispersions. Such resolution achieved for an interface buried behind a ~ 18 -Å-thick overlayer presents the forefront of nowadays SX-ARPES instrumentation. The temperature dependence was measured with increasing temperature to avoid possible hysteresis effects⁵⁴.

First-principles calculations. Band structure calculations for the LAO/STO interface were performed using the pseudo-self-interaction correction method⁵⁵, with a plane wave basis set and ultrasoft pseudopotentials. This *ab initio* approach corrects the main deficiencies of basic density functional theory for a vast range of oxides⁸. The theoretical band structure and the FS were calculated for an interfacial carrier density of 0.115 electrons per u.c. This value is consistent with those determined using Hall effect measurements for the LAO/STO interface. The corresponding Fermi momentum k_F of the d_{yz} -states is in good agreement with the experimental value of $\sim 0.29 \text{ \AA}^{-1}$ determined as the highest band dispersion point.

DFT-based phonon calculations under different electron doping were performed using the VASP code⁵⁷. The electron count was adjusted while adding a compensating background charge. We used the PBEsol functional, which gives reliable lattice parameters and phonon frequencies⁵⁶, and PAW potentials⁵⁷ with Sr(4s,4p,5s), Ti(3p,3d,4s) and O(2s,2p) valence shells. Phonons were then computed using the frozen phonon approach⁵⁸. For further details, see ref. 50.

References

- Mahan, G. D. *Many Particle Physics* (Plenum, 1981).
- Holstein, T. Studies of polaron motion. *Ann. Phys. (N.Y.)* **8**, 343–389 (1959).
- Das Sarma, S. & Stopa, M. Phonon renormalization effects in quantum wells. *Phys. Rev. B* **36**, 9595–9603 (1987).
- Strocov, V. N. *et al.* Soft-X-ray ARPES at the Swiss Light Source: from 3D materials to buried interfaces and impurities. *Synchr. Rad. News* **27**, 31–40 (2014).
- Hwang, H. Y. *et al.* Emergent phenomena at oxide interfaces. *Nat. Mater.* **11**, 103–113 (2012).
- Mannhart, J. & Schlom, D. G. Oxide interfaces—an opportunity for electronics. *Science* **327**, 1607–1611 (2010).
- Ohtomo, A. & Hwang, H. Y. A high-mobility electron gas at the LaAlO₃/SrTiO₃ heterointerface. *Nature* **427**, 423–426 (2004).
- Delugas, P. *et al.* Spontaneous 2-dimensional carrier confinement at the n-Type SrTiO₃/LaAlO₃ Interface. *Phys. Rev. Lett.* **106**, 166807 (2011).
- Son, W.-J., Cho, E., Lee, B., Lee, J. & Han, S. Density and spatial distribution of charge carriers in the intrinsic n-type LaAlO₃-SrTiO₃ interface. *Phys. Rev. B* **79**, 245411 (2009).
- Dubroka, A. *et al.* Dynamical response and confinement of the electrons at the LaAlO₃/SrTiO₃ interface. *Phys. Rev. Lett.* **104**, 156807 (2008).
- Salluzzo, M. *et al.* Orbital reconstruction and the two-dimensional electron gas at the LaAlO₃/SrTiO₃ interface. *Phys. Rev. Lett.* **102**, 166804 (2014).
- Santander-Syro, A. F. *et al.* Two-dimensional electron gas with universal subbands at the surface of SrTiO₃. *Nature* **469**, 189–193 (2011).
- King, P. D. C. *et al.* Quasiparticle dynamics and spin-orbital texture of the SrTiO₃ two-dimensional electron gas. *Nat. Commun.* **5**, 3414 (2014).
- Cancellieri, C. *et al.* Doping-dependent band structure of LaAlO₃/SrTiO₃ interfaces by soft x-ray polarization-controlled resonant angle-resolved photoemission. *Phys. Rev. B* **89**, R121412 (2014).
- Fête, A. *et al.* Large modulation of the Shubnikov-de Haas oscillations by the Rashba interaction at the LaAlO₃/SrTiO₃ interface. *New J. Phys.* **16**, 112002 (2014).
- Banerjee, S., Erten, O. & Randeria, M. Ferromagnetic exchange, spin-orbit coupling and spiral magnetism at the LaAlO₃/SrTiO₃ interface. *Nat. Phys.* **9**, 626–630 (2013).
- Caviglia, A. D. *et al.* Tunable Rashba spin-orbit interaction at oxide interfaces. *Phys. Rev. Lett.* **104**, 126803 (2010).
- Gariglio, S., Reyren, N., Caviglia, A. D. & Triscone, J.-M. Superconductivity at the LaAlO₃/SrTiO₃ interface. *J. Phys. Condens. Matter* **21**, 164213 (2009).
- Cancellieri, C. *et al.* Influence of the growth conditions on the LaAlO₃/SrTiO₃ interface electronic properties. *Europhys. Lett.* **91**, 17004 (2010).
- Thiel, S., Hammerl, G., Schmehl, A., Schneider, C. W. & Mannhart, J. Tunable quasi-two-dimensional electron gases in oxide heterostructures. *Science* **313**, 1942–1945 (2006).
- Molodtsov, S. L. *et al.* Angle-resolved resonant photoemission as a probe of spatial localization and character of electron states. *Phys. Rev. Lett.* **78**, 142 (1997).
- Cancellieri, C. *et al.* Interface Fermi states of LaAlO₃/SrTiO₃ and related heterostructures. *Phys. Rev. Lett.* **110**, 137601 (2013).
- Berner, G. *et al.* Direct \mathbf{k} -space mapping of the electronic structure in an oxide-oxide interface. *Phys. Rev. Lett.* **110**, 247601 (2013).
- Moser, S. *et al.* Tunable polaronic conduction in anatase TiO₂. *Phys. Rev. Lett.* **110**, 196403 (2013).
- Mishchenko, A. S. & Nagaosa, N. Electron-phonon coupling and a polaron in the $t - J$ model: from the weak to the strong coupling regime. *Phys. Rev. Lett.* **93**, 036402 (2004).
- Mishchenko, A. S. *et al.* Polaronic metal in lightly doped high-Tc cuprates. *Europhys. Lett.* **95**, 57007 (2011).
- Verbist, G., Peeters, F. M. & Devreese, J. T. Extended stability region for large bipolarons through interaction with multiple phonon branches. *Ferroelectrics* **130**, 27–34 (1992).
- Meevasana, W. *et al.* Strong energy-momentum dispersion of phonon-dressed carriers in the lightly doped band insulator SrTiO₃. *New J. Phys.* **12**, 023004 (2010).
- Cardona, M. Optical properties and band structure of SrTiO₃ and BaTiO₃. *Phys. Rev. A* **140**, 651 (1965).
- Choudhury, N., Walter, E. J., Kolesnikov, A. I. & Loong, C.-K. Large phonon band gap in SrTiO₃ and the vibrational signatures of ferroelectricity in ATiO₃ perovskites: First-principles lattice dynamics and inelastic neutron scattering. *Phys. Rev. B* **77**, 134111 (2008).
- van Mechelen, J. L. M. *et al.* Electron-phonon interaction and charge carrier mass enhancement in SrTiO₃. *Phys. Rev. Lett.* **100**, 226403 (2010).
- Chang, Y. J., Bostwick, A., Kim, Y. S., Horn, K. & Rotenberg, E. Structure and correlation effects in semiconducting SrTiO₃. *Phys. Rev. B* **81**, 235109 (2010).
- Wang, Z. *et al.* Tailoring the nature and strength of electron-phonon interactions in the SrTiO₃(001) two-dimensional electron liquid. Preprint at <http://arxiv.org/abs/1506.01191> (2015).
- Chen, C., Avila, J., Frantzeskakis, E., Levy, A. & Asensio, M. C. Observation of a two-dimensional liquid of Fröhlich polarons at the bare SrTiO₃ surface. *Nat. Commun.* **6**, 8585 (2015).

35. Jia, C. L. *et al.* Oxygen octahedron reconstruction in the SrTiO₃/LaAlO₃ heterointerfaces investigated using aberration-corrected ultrahigh-resolution transmission electron microscopy. *Phys. Rev. B* **79**, 081405(R) (2009).
36. Doennig, D. & Pentcheva, R. Control of orbital reconstruction in (LaAlO₃)_M/(SrTiO₃)_N(001) quantum wells by strain and confinement. *Sci. Rep.* **20**, 7909 (2015).
37. Pallecchi, I. *et al.* Giant oscillating thermopower at oxide interfaces. *Nat. Commun.* **6**, 6678 (2015).
38. Mishchenko, A. S., Nagaosa, N. & Prokof'ev, N. Diagrammatic Monte Carlo method for many-polaron problems. *Phys. Rev. Lett.* **113**, 166402 (2014).
39. Breitschaft, M. *et al.* Two-dimensional electron liquid state at LaAlO₃-SrTiO₃ interfaces. *Phys. Rev. B* **81**, 153414 (2010).
40. Feng, G. S. & White, S. R. Numerical study of the spectral weight function for the half-filled two-dimensional Hubbard model. *Phys. Rev. B* **46**, 8691(R) (1992).
41. Mishchenko, A. S., Nagaosa, N., De Filippis, G., de Candia, A. & Cataudella, V. Mobility of Holstein polaron at finite temperature: an unbiased approach. *Phys. Rev. Lett.* **114**, 146401 (2015).
42. Mannella, N. *et al.* Polaron coherence condensation as the mechanism for colossal magnetoresistance in layered manganites. *Phys. Rev. B* **76**, 233102 (2007).
43. Hao, X., Wang, Z., Schmid, M., Diebold, U. & Franchini, C. Coexistence of trapped and free excess electrons in SrTiO₃. *Phys. Rev. B* **91**, 085204 (2015).
44. Mishchenko, A. S. *et al.* Localization-delocalization transition of a polaron near an impurity. *Phys. Rev. B* **79**, 180301(R) (2009).
45. Chen, Y. Z. *et al.* A high-mobility two-dimensional electron gas at the spinel/perovskite interface of γ -Al₂O₃/SrTiO₃. *Nat. Commun.* **4**, 1371 (2013).
46. Braun, J. *et al.* Exploring the XPS limit in soft and hard x-ray angle-resolved photoemission using a temperature-dependent one-step theory. *Phys. Rev. B* **88**, 205409 (2013).
47. Wang, F. F. Y. & Gupta, K. P. Phase transformation in the oxides. *Mettall. Trans.* **4**, 2767 (1973).
48. Müller, K. A. & Burkard, H. SrTiO₃: an intrinsic quantum paraelectric below 4K. *Phys. Rev. B* **19**, 3593 (1979).
49. Vanderbilt, D. & Zhong, W. First-principles theory of structural phase transitions for perovskites: competing instabilities. *Ferroelectrics* **206**, 181–204 (1998).
50. Aschauer, U. & Spaldin, N. A. Competition and cooperation between antiferrodistortive and ferroelectric instabilities in the model perovskite SrTiO₃. *J. Phys. Condens. Matter* **26**, 122203 (2014).
51. Mishchenko, A. S., Prokof'ev, N. V., Sakamoto, A. & Svistunov, B. V. Diagrammatic quantum Monte Carlo study of the Fröhlich polaron. *Phys. Rev. B* **62**, 6317 (2000).
52. Boschker, H., Richter, C., Fillis-Tsirakis, E., Schneider, C. W. & Mannhart, J. Electron-phonon coupling and the superconducting phase diagram of the LaAlO₃-SrTiO₃ interface. *Sci. Rep.* **5**, 12309 (2015).
53. Strocov, V. N. *et al.* Soft-X-ray ARPES facility at the ADDRESS beamline of the SLS: Concepts, technical realisation and scientific applications. *J. Synchrotron Rad.* **21**, 32–44 (2014).
54. Schoofs, F., Egilmez, M., Fix, T., MacManus-Driscoll, J. L. & Blamire, M. G. Impact of structural transitions on electron transport at LaAlO₃/SrTiO₃ heterointerfaces. *Appl. Phys. Lett.* **100**, 081601 (2012).
55. Filippetti, A. *et al.* Introducing a variational pseudo-self-interaction correction approach for solids and molecules. *Phys. Rev. B* **84**, 195127 (2011).
56. Wahl, R., Vogtenhuber, D. & Kresse, G. SrTiO₃ and BaTiO₃ revisited using the projector augmented wave method: Performance of hybrid and semilocal functionals. *Phys. Rev. B* **78**, 104116 (2008).
57. Kresse, G. & Joubert, D. From ultrasoft pseudopotentials to the projector augmented-wave method. *Phys. Rev. B* **59**, 1758–1775 (1999).
58. Togo, A., Oba, F. & Tanaka, I. First-principles calculations of the ferroelastic transition between rutile-type and CaCl₂-type SiO₂ at high pressures. *Phys. Rev. B* **78**, 134106 (2008).

Acknowledgements

We thank P.R. Willmott, J.H. Dil, R. Claessen, J.-M. Triscone, F. Baumberger, F. Bisti, Z. Wang, M. Radović, J. Mesot and N.A. Spaldin for fruitful discussions, and X. Wang for software support of the experiment. Parts of this research were supported by the ImPACT Program of the Council for Science, Technology and Innovation (Cabinet Office, Government of Japan), the Croatian QuantiXLie Center of Excellence, and the ETH Zürich and ERC Advanced Grant program, No. 291151.

Author contributions

C.C. and V.N.S. have performed the experiment supported by V.A.R. and T.S. and processed the data. C.C. has grown the samples. V.N.S. and A.S.M. have developed the scientific concept. A.S.M. has performed the polaronic analysis supported by O.S.B. and N.N. A.F. and U.A. have calculated the electron and phonon band structures, respectively. All authors have discussed the results and interpretations, as well as the manuscript written by V.N.S. and A.S.M. with contributions of C.F., U.A. and C.C.

Additional information

Supplementary Information accompanies this paper at <http://www.nature.com/naturecommunications>

Competing financial interests: The authors declare no competing financial interests.

Reprints and permission information is available online at <http://npg.nature.com/reprintsandpermissions/>

How to cite this article: Cancellieri, C. *et al.* Polaronic metal state at the LaAlO₃/SrTiO₃ interface. *Nat. Commun.* **7**:10386 doi: 10.1038/ncomms10386 (2016).



This work is licensed under a Creative Commons Attribution 4.0 International License. The images or other third party material in this article are included in the article's Creative Commons license, unless indicated otherwise in the credit line; if the material is not included under the Creative Commons license, users will need to obtain permission from the license holder to reproduce the material. To view a copy of this license, visit <http://creativecommons.org/licenses/by/4.0/>